



# Signatures of Intermittency and Fine-scale Turbulence in the Very Local Interstellar Medium

Federico Fraternali<sup>1</sup> , Nikolai V. Pogorelov<sup>1,2</sup> , and Leonard F. Burlaga<sup>3</sup> <sup>1</sup> Center for Space Plasma and Aeronomic Research, University of Alabama in Huntsville, Huntsville, AL 35805, USA; [federico.fraternali@uah.edu](mailto:federico.fraternali@uah.edu)<sup>2</sup> Department of Space Science, University of Alabama in Huntsville, Huntsville, AL 35805, USA<sup>3</sup> MC 673, NASA Goddard Space Flight Center, Greenbelt, MD 20771, USA

Received 2020 May 18; revised 2020 June 17; accepted 2020 June 18; published 2020 July 9

## Abstract

This study presents the first Voyager 1 (V1) observation of magnetic turbulence intermittency and fine-scale structures associated with the propagation of a shock wave in the outer heliosheath. The intermittent event starts on DOY 178 in 2014 upstream of the shock wave that overtook V1 on DOY 237 at 140 au from the Sun. The distribution of magnetic field increments follows the  $q$ -Gaussian distribution with the index  $q \approx 1.57$  for the maximum variance component. Evidence is provided of fine-scale structures well below the Coulomb collisional scale. They undergo a turbulent cascade at scales less than  $10^{-3}$  au. Observed magnetohydrodynamic fluctuations show signatures of irregular filamentary structures, sawtooth-like waveforms of mixed compressible/transverse nature, which evolve into shocklets and current sheets. Observational data challenges the interpretation of the interstellar plasma in the outer heliosheath as a featureless medium at scales below the collisional mean free path of about 1 au. These results are of importance for better understanding of turbulent processes in the outer heliosheath, including magnetic reconnection, shock-turbulence interaction, Galactic cosmic-ray transport, plasma wave generation, and radio emission.

*Unified Astronomy Thesaurus concepts:* [Interstellar magnetic fields \(845\)](#); [Heliopause \(707\)](#); [Heliosphere \(711\)](#)

## 1. Introduction

The very local interstellar medium (VLISM) is the part of the LISM affected by the presence of the heliosphere. The heliospheric boundary layer (HBL) is the VLISM region immediately adjacent to the heliopause (HP), where charge-exchange-driven, kinetic effects create a layer of decreased plasma density observed by Voyager 1 (V1; Gurnett et al. 2015; Zank 2015; Pogorelov et al. 2017b). The HBL is a dynamic region crossed by shocks traveling outwards into the VLISM (Burlaga & Ness 2016; Kim et al. 2017). V1 has been sampling the HBL since 2012 August (Stone et al. 2013). Voyager 2 (V2) crossed the HP, in 2018 November (see, e.g., Burlaga et al. 2019a; Richardson et al. 2019).

Shocks and pressure pulses in the solar wind (SW) cause 1–2 au oscillations of the HP and penetrate into the VLISM (Gurnett et al. 2013, 2015; Richardson 2016; Pogorelov et al. 2017a; Burlaga et al. 2019b). Three major shock/compression wave events were detected by V1 in 2012.92, 2014.65, and 2017.0, and have been reproduced rather well by simulations (Kim et al. 2017). Magnetic field fluctuations in the HBL have been found by Burlaga et al. (2015) to be relatively weak and compressible, with a Kolmogorov-like spectral decay, suggesting their turbulent nature. Further analysis (Burlaga et al. 2018) of the 2015/2016 data revealed the presence of large-scale Alfvénic fluctuations. Possible mechanisms of wave transmission and subsequent mode conversion have been proposed by Zank et al. (2017, 2019) and Matsukiyo et al. (2019).

Fraternali et al. (2019a), by analyzing kurtosis of the magnetic field distributions measured by V1 demonstrated the presence of intermittency in measured VLISM turbulence on timescales exceeding 1 hr and extending to the Sun’s rotation period. Here we perform spectral and higher-order statistics analyses of 48 s magnetic field data collected by V1 and

demonstrate the presence of intermittency in high-frequency data, and local phenomena in front of a traveling shock.

Fluctuations measured by V1 have maximum amplitude of about 0.1 of the magnetic field strength,  $|B|$ , on timescales from 48 s to 1 hr. This corresponds to microscale turbulence in the MHD-to-kinetic transitional regime. The time interval we choose is appropriate because (i) the intermittency is a necessary feature of strong turbulence and (ii) the event we consider involves a precursor of the 2014.65 shock wave. We focus on the event that occurred 44 days after V1 entered the electron foreshock region on DOY 134 of 2014. This event is also associated with (1) the Galactic cosmic-ray (GCR) flux variations measured by the CRS and LECP instruments and (2) plasma wave and radio emission observations by the Plasma Wave Instrument (PWS; Gurnett et al. 2015).

## 2. Voyager 1 Observations

We analyze V1 magnetic field data averaged over 48 s, the highest resolution available. The vector components are presented in the spacecraft-centered,  $RTN$  frame. The  $R$ -axis is directed radially outward from the Sun, the  $T$ -axis is parallel to the Sun’s equatorial plane and aligned with the direction of the Sun’s rotation, while the  $N$ -axis completes the right coordinate system. The estimated  $1\sigma$  uncertainties in the 2014 data, including the systematic calibration errors and noise, are  $\pm 0.02$  nT for the  $T$ - and  $N$ -components, and up to 0.1 nT for the  $R$ -component (Berdichevsky 2009). Limited telemetry coverage results in  $\sim 70\%$  data loss, with periodic data gaps of 8–16 hr per day, which seriously compromise the multiscale analysis in the range of spacecraft frequencies  $10^{-5} \lesssim f \lesssim 10^{-4}$  Hz.

The upper panel of Figure 1 shows V1 measurements of the magnetic field magnitude over the time interval from 2014 to 2015.5. The shock under consideration overtook V1 in

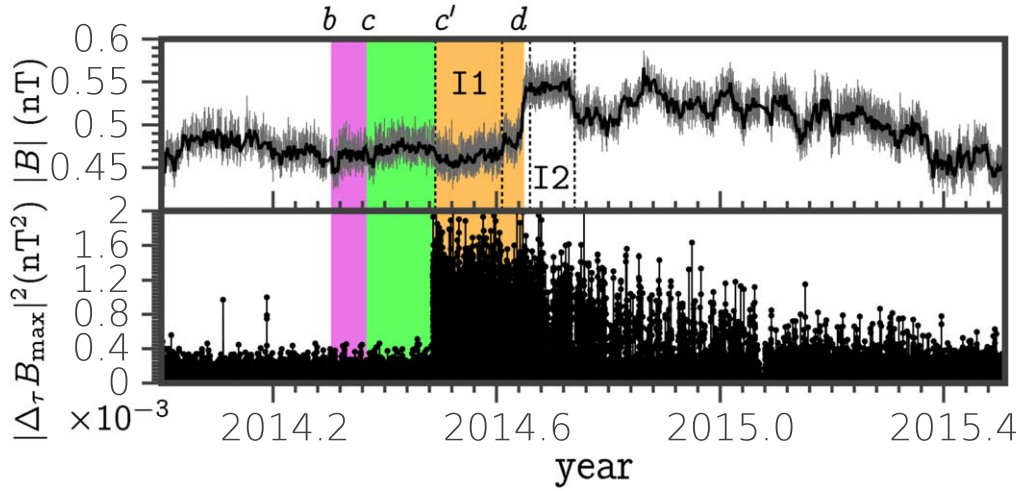


**Figure 1.** Shock propagating through the VLISM in 2014. We highlight the region of GCR flux enhancement (purple) and the region of intense and spiky plasma waves (green). The orange band indicates the region of enhanced MHD fluctuations, also shown in the lower panel in terms of increments of  $B_{\max}$ . Labels  $b$ ,  $c$ , and  $d$  (Gurnett et al. 2015) denote the outer boundaries of the GCR and electron foreshocks, and the shock itself (DOY 111, 134, and 236, respectively). Label  $c'$  marks the boundary of the ion foreshock (DOY 178).

2014.65. The bottom panel shows the normalized squared increments of the maximum variance magnetic field component  $B_{\max}$  (see Section 3). One can see a remarkable amplification of magnetic field fluctuations (10% of the mean field) that starts on DOY 178 and gradually decreases in the downstream region until the beginning of 2015. Notice the consecutive moments of time when V1 is crossed by the GCR, electron, and ion foreshocks.

We select the time intervals upstream and downstream of the shock, hereinafter referred to as  $\text{I1}$  and  $\text{I2}$ . Interval  $\text{I1}$  extends from DOY 178 to DOY 223, and contains 85 contiguous segments with an average length of 4.66 hr. The unit vector in the average direction of  $\mathbf{B}$  is  $\hat{e}_{\parallel} = (0.41, -0.84, 0.36)$ . The direction of the maximum variance vector is  $\hat{e}_{\max} = (0.017, 0.60, 0.80)$ . Both directions are given in the  $RTN$  frame. Thus, the angle between these two vectors is  $\theta_{\hat{e}_{\parallel}, \hat{e}_{\max}} \approx 102^{\circ}.4$ . The angles that  $\hat{e}_{\max}$  and  $\hat{e}_{\min}$  make with the radial direction ( $\hat{e}_R$ ) are  $\theta_{\hat{e}_R, \hat{e}_{\max}} \approx 98^{\circ}$  and  $\theta_{\hat{e}_R, \hat{e}_{\min}} \approx 8^{\circ}.5$ . Interval  $\text{I2}$  is from DOY 242 to DOY 271 immediately downstream of the shock. This interval includes 45 segments with the average length of 3.64 hr. Inside  $\text{I2}$ ,  $\hat{e}_{\parallel} = (0.34, -0.86, 0.37)$  and  $\hat{e}_{\max} = (0.03, 0.57, 0.82)$ , so that  $\theta_{\hat{e}_{\parallel}, \hat{e}_{\max}} \approx 102^{\circ}.0$ ,  $\theta_{\hat{e}_R, \hat{e}_{\max}} \approx 88^{\circ}$ , and  $\hat{e}_{\min} \approx \hat{e}_R$ . An analysis of quantities near this shock was given by Burlaga & Ness (2016). This shock is quasi-perpendicular ( $\theta_{\hat{n}, \hat{e}_{\parallel}} \approx 65^{\circ}$ ) and propagates nearly radially ( $\theta_{\hat{n}, \hat{e}_R} \approx 16^{\circ}$ ). The compression ratio is  $n_{\text{I2}}/n_{\text{I1}} = 1.11 \approx B_{\text{I2}}/B_{\text{I1}} = 1.13$ , where  $n = n_e = n_p$  is the plasma number density. The densities  $n_{\text{I1}} \approx 0.0873 \text{ cm}^{-3}$  and  $n_{\text{I2}} \approx 0.0968 \text{ cm}^{-3}$  are indirectly obtained from the V1 PWS data (Gurnett et al. 2015). To estimate the missing plasma parameters, we assume the upstream temperature and radial bulk flow velocity to be  $T_{\text{I1}} = 30,000 \text{ K}$  ( $T = T_p = T_e$ ) and  $U_{\text{I1}} = -12 \text{ km s}^{-1}$ , respectively. We also choose the shock velocity to be  $40 \text{ km s}^{-1}$  (Kim et al. 2017). The chosen temperature is higher than that used by Burlaga & Ness (2016; 20,000 K), but it is in better agreement with the recent observations of V2 (Richardson et al. 2019) and simulations (Pogorelov et al. 2015). Thus, the sound speed, Alfvén velocity, and fast magnetosonic velocity in the direction perpendicular to  $\mathbf{B}$  in the upstream region are

$C_s = \sqrt{\gamma k_B (2T)/m_p} \approx 28.7 \text{ km s}^{-1}$ ,  $C_A \approx 35.2 \text{ km s}^{-1}$ , and  $C_F = \sqrt{C_s^2 + C_A^2} \approx 45.4 \text{ km s}^{-1}$ , respectively. The plasma beta is  $\beta = nk_B(T_e + T_p)/(B^2/2\mu_0 m_p n) \approx 0.82$ . This makes a fast, subcritical shock with respective Mach numbers  $M_s \approx 1.8$ ,  $M_A \approx 1.5$ , and  $M_F \approx 1.2$ . For a nearly perpendicular shock, the Rankine–Hugoniot conditions give a jump of  $\sim 5 \text{ km s}^{-1}$  in the radial velocity component. Thus, the downstream bulk flow speed in the fixed frame,  $U_{\text{I2}}$ , is  $\sim -7 \text{ km s}^{-1}$ .

The thermal proton gyroradii are  $r_{cp, \text{I1}} \approx 345 \text{ km}$  and  $r_{cp, \text{I2}} \approx 329 \text{ km}$ , respectively. The proton gyrofrequencies are  $f_{cp, \text{I1}} \approx 7.3 \times 10^{-4} \text{ Hz}$  and  $f_{cp, \text{I2}} \approx 8.1 \times 10^{-4} \text{ Hz}$ . The electron plasma frequencies are  $f_{pe, \text{I1}} \approx 2650$  and  $f_{pe, \text{I2}} \approx 2790 \text{ Hz}$ .

### 3. Results

A remarkable increase in transverse magnetic field fluctuations shown in Figure 1 starts on DOY 178 about 1.4 au ahead of the shock front. Figure 2 shows two subsets within  $\text{I1}$  (panels (a) and (b)) and  $\text{I2}$  (panels (c) and (d)). Panels (e) and (f) refer to the shaded regions identified in the leftmost panels.

Given the  $1\sigma$  uncertainty it appears that most fine-scale VLISM fluctuations fall into the noisy band, which makes it challenging to identify physical processes hidden in data. In these specific intervals, however, the most intense fluctuations are transverse and reach values as high as 0.06 nT, which is above the noise threshold for the  $T$ - and  $N$ -components. Most of the steepest variations occur smoothly within a few 48 s data points. The correlation between  $\delta B_T$  and  $\delta B_N$  is  $\approx 0.4$  (see Figure 2), ruling out the possibility that the observed fluctuations are statistical and/or instrumental artifacts. Although it is impossible to quantify the effect of spacecraft-generated fields, our analyses suggest that we are dealing with realistic phenomena.

It appears that  $B_{\max}$  is nearly transverse and experiences rapid variations, with profiles resembling irregular square waves, usually not seen in the field strength, which suggests the presence of small-amplitude “directional discontinuities” (Burlaga 1969).

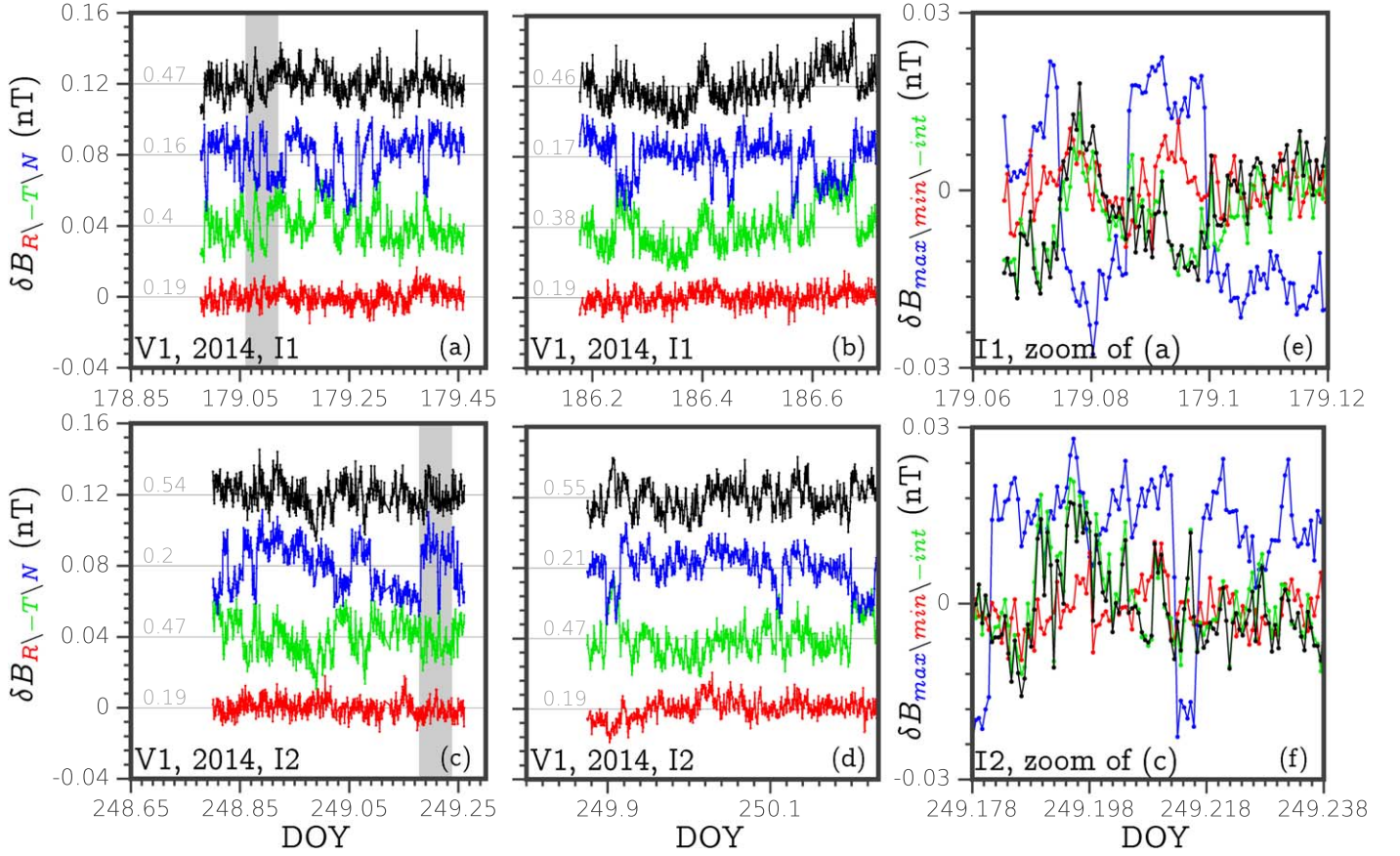


**Figure 2.** Magnetic field fluctuations in subintervals of I1 (top) and I2 (bottom). Panels (a)–(d) show the  $R$ -,  $T$ -, and  $N$ -components. Red and blue curves show  $\delta B_R$  and  $\delta B_T$ . Notice that  $\delta B_T$  is shown with the opposite sign for convenience. The field magnitude is shown with black lines. A shift of 0.04 nT is applied between the components. The mean values are indicated on top of the horizontal gray lines. Panels (e) and (f) show a 3 hr zoom into the gray bands indicated in panels (a) and (c), the maximum variance frame being used.

We analyze the partial variance of increments (PVI) of magnetic field (Figures 3(b), (d)). This approach is extensively used in the SW data analysis as tool for detection of intermittent structures (Greco et al. 2008; Bruno & Carbone 2013). Here we use the following definition of PVI:

$$\text{pvi}_\tau[\mathbf{B}](t; \tau) = |\Delta_\tau \mathbf{B}|^2 / \langle |\Delta_\tau \mathbf{B}|^2 \rangle, \quad (1)$$

where  $\Delta_\tau \mathbf{B}(t; \tau) = \mathbf{B}(t) - \mathbf{B}(t + \tau)$  defines the increments with temporal separations  $\tau$ . It is also useful to look at the angle between fluctuations separated by  $\tau$ ,

$$\theta_\tau = \cos^{-1}[\delta \mathbf{B}(t) \cdot \delta \mathbf{B}(t + \tau) / (|\delta \mathbf{B}(t)| |\delta \mathbf{B}(t + \tau)|)]. \quad (2)$$

In Figure 3, the PVIs are computed separately for  $B_{\max}$  and  $|\mathbf{B}|$ , using  $\tau = 144$  s. For the most intense events,  $\text{pvi}_\tau[B_{\max}]$  reaches values up to 35, while the fluctuation vector  $\delta \mathbf{B}$  rotates by  $\theta_\tau$  up to  $160^\circ$ . These high-shear events are abundant, as seen from red spikes in Figure 3 (top panels), and indicate directional discontinuities. This can be inferred by examining the location of black spikes indicating compressible events.

The time  $t_p$  for these weak discontinuities to pass V1 is from two to six 48 s intervals (see Figures 2(e) and (f)). It is impossible to infer the exact geometry of these structures from 1D data, especially if some quantities are missing. One of the possibilities is that V1 observed weak tangential discontinuities exhibiting local slab geometry (the actual topology is likely filamentary). Then, the normal vector would be orthogonal to the plane containing the initial and final field, on average  $\hat{\mathbf{n}} = (0.89 \pm 0.03, 0.33 \pm 0.07, -0.24 \pm 0.14) \approx \hat{\mathbf{e}}_{\max} \times \hat{\mathbf{e}}_{\parallel}$

and  $(0.92 \pm 0.02, 0.27 \pm 0.07, -0.22 \pm 0.15)$  for I1 and I2, respectively.

Assuming that these discontinuities propagate with the bulk flow with relative radial velocity  $V_{\text{rel}} = |U_{R,I1} - V_{\text{SC}}| \approx 30 \text{ km s}^{-1}$ , the thickness becomes  $\Delta \approx V_{\text{rel}} t_p \approx 3000\text{--}7500 \text{ km}$ , or  $8\text{--}20 r_{cp}$ . Although the origin of the current sheets (CS) is definitely local, their normalized width is in remarkable agreement with the average scale of CSs associated with pressure balanced structures in the supersonic SW and inner heliosheath (IHS; Burlaga et al. 1977; Burlaga & Ness 2011). Statistical analysis of time intervals between consecutive occurrences (waiting times,  $t_w$ ) of intermittent events ( $\text{pvi}[B_{\max}] > 12$ ) reveals a broad probability density function (PDF) that fits the power law with the index of  $\approx -1 \pm 0.1$  both upstream and downstream of the shock, in the range of  $t_w \in [600, 4000]$  s. The average passing times for V1 are 2930 s and 3220 s ( $\sim 246 r_{cp}$  and  $235 r_{cp}$ ) in I1 and I2, respectively. Interestingly, very similar statistics characterize MHD turbulence with small-scale sheets and high-shear regions (e.g., Matthaeus et al. 2015). Small-scale reconnections may occur for a fraction of these CSs. The ratio  $\langle t_{w,I2} \rangle / \langle t_{w,I1} \rangle = 1.10$  is consistent with the expected compression of filaments across the shock, estimated as  $\langle t_{w,I2} \rangle / \langle t_{w,I1} \rangle \approx f_{\text{SC},I1} / f_{\text{SC},I2} \approx (1/r) [|U_{I1} - V_{\text{SC}}| / |V_{\text{SH}} - r(V_{\text{SH}} - U_{I1}) - V_{\text{SC}}|] \approx 1.09$ .

Magnetic compressibility and magnetic pressure fluctuations are given in the upper panels of Figure 3. We used two

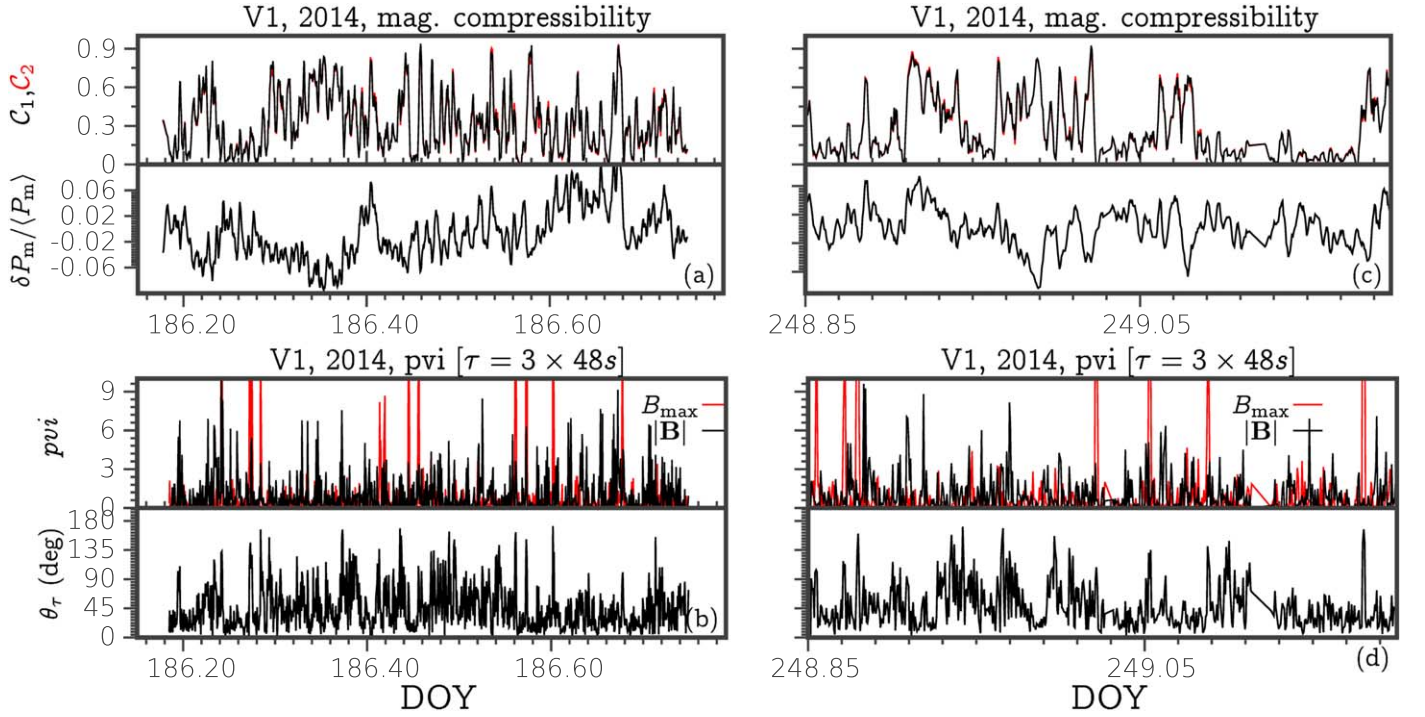


**Figure 3.** Top panels: magnetic compressibility and normalized magnetic pressure fluctuations. Bottom panels: the PVIs of the maximum variance component  $B_{\max}$  (red lines) and field strength  $|\mathbf{B}|$  (black lines), for  $\tau = 144$  s (PVIs exceed 30 for the most intense events). The lower subpanels display the angle between fluctuations separated by 144 s.

indicators for the fraction of turbulent magnetic energy of fluctuations parallel to the mean magnetic field:

$$C_1 = \left( \frac{\langle \mathbf{B} \rangle_\tau \cdot \delta \mathbf{B}}{\langle \mathbf{B} \rangle_\tau \delta B} \right)^2, \quad C_2 = \left( \frac{\delta |\mathbf{B}|}{|\delta \mathbf{B}|} \right)^2, \quad (3)$$

where  $\langle \bullet \rangle_\tau$  is a low-pass filter with the window of  $\tau = 3$  days. Besides,  $\delta(\bullet) = (\bullet) - \langle \bullet \rangle_\tau$ . These two indicators give very close results.

The average magnetic compressibility is around 32% due to large  $\delta B_{\max}$  fluctuations. However, relatively large ( $\sim 10\%$ ) and sharp variations in magnetic pressure ( $P_{\text{mag}}$ ) are also present. Although these fluctuations are mostly in the noise bin, the similarity of their profiles and known coherent structures (Tsurutani & Stone 1985; Burlaga 1995) suggests that these processes are truly occurring in the VLISM. The profiles vary, exhibiting repeated patterns consistent with the presence of mixed compressible/transverse MHD fluctuations, which are expected (Kim et al. 2017; Matsukiyo et al. 2019) to undergo nonlinear steepening and interaction, and may evolve into shocklets. The field is likely a superposition of preexisting upstream turbulence and MHD fluctuations induced by shock-related kinetic processes. The direction of propagation of such packets and their physical origin are not well understood. However, the Doppler shift ( $\kappa V_{\text{rel}}$ ) for field-aligned Alfvén wave propagation, sonic, and advective modes provides us with similar estimates of spatial scales.

We conclude that the small-scale magnetic field is intermittent. This is seen from the PDFs of magnetic field increments shown in Figure 4. Because of the turbulence anisotropy, intermittency is observed predominantly in transverse fluctuations. One cannot exclude that intermittency of longitudinal fluctuations is below the noise threshold. We fit the PDFs with a  $q$ -Gaussian distribution (Tsallis 1988),

exhibiting a Gaussian core and power-law tails

$$f_q(\Delta B_j/\sigma) = A_q [1 + (q-1)\beta_q(\Delta B_j/\sigma)^2]^{-\frac{1}{q-1}}. \quad (4)$$

It is known that the increments of turbulent fluctuations in the remote SW and IHS are fit excellently by  $q$ -Gaussian distributions (Burlaga et al. 2013) with  $q$  as large as 1.7. Remarkably, we find  $q = 1.57$  and  $1.50 (\pm 0.02)$  for the increments of  $\Delta B_{\max}$ , in intervals  $\mathbb{I}1$  and  $\mathbb{I}2$ , respectively. Such values correspond to kurtosis  $\mathcal{K} = 9.1$  and  $8$ , respectively. On the contrary,  $\Delta B_{\min}$  and  $\Delta B_{\text{int}} \approx \Delta |\mathbf{B}|$  display almost Gaussian statistics. This results in  $q \approx 1.35$  and  $1.2$  for  $\Delta B_N$  and  $\Delta B_T$ , respectively.

Reduced power spectral densities,  $P$ , of magnetic field are shown in Figure 5 for spacecraft frequencies  $f \in [10^{-7}, 10^{-2}]$  Hz. We also provide wavenumbers estimated using the Taylor (1938) approximation based on the radial component of the bulk plasma flow velocity with respect to the spacecraft and assuming that (i)  $\kappa_\perp \gg \kappa_\parallel$ , (ii) the plasma-frame frequency associated with nonlinear deformation is much smaller than the Doppler shift, and (iii) the wave dispersion is not yet dominant. In fact, the inequality  $\omega_{nl} \lesssim \delta v_{\max} \kappa \lesssim (3 \text{ km s}^{-1}) \kappa < \kappa \cdot \mathbf{V}_{\text{rel}}$  is satisfied for most wavenumbers. For traveling wave modes, this approximation could be violated.

The PSDs are estimated using different techniques and occasional generation of synthetic turbulence data to fix artifacts introduced by missing data (Gallana et al. 2016; Fraternali et al. 2019a, 2019b). Averaging of the spectra computed from the contiguous subsamples allows us to investigate the frequency range  $f \gtrsim 10^{-4}$  Hz.

Surprisingly, a Kolmogorov-like spectrum is observed in this range ( $10^{-2} \lesssim \kappa r_{cp} \lesssim 1$ ). In  $\mathbb{I}1$ , the fit computed for  $f \in [1.5 \times 10^{-4}, 6 \times 10^{-4}]$  Hz gives  $P \propto f^{-\alpha}$  with  $\alpha = 0.8, 1.33, 1.55$ , and  $1.42$  for the  $R$ -,  $T$ -, and  $N$ -components, and for

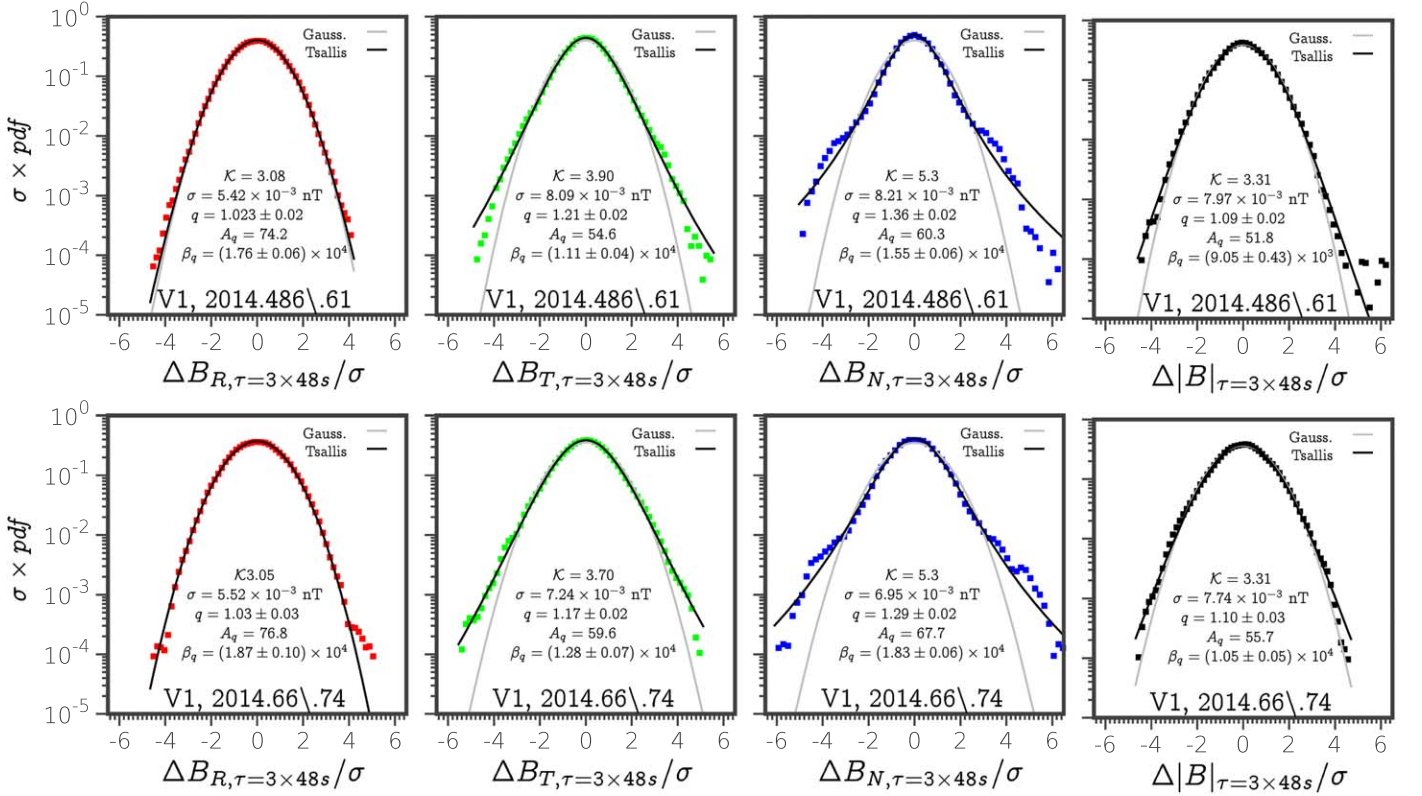


**Figure 4.** Normalized PDFs of magnetic field increments for  $\tau = 3 \times 48$  s. Top row: interval I1. Bottom row: interval I2. Left to right: the  $R$ -,  $T$ -, and  $N$ -components, and  $|B|$ . All panels show the empirical distributions (squares) and fits by both the Gaussian and  $q$ -Gaussian distributions (gray and black lines, respectively). The parameters of the  $q$ -Gaussian fit are also shown.

the trace  $E_m = \sum_3 P[B_j]$ , respectively. The fit uncertainty is about  $\pm 0.03$ . In I2, the spectrum is steeper ( $\alpha = 0.76, 1.47, 1.65$ , and  $1.52$ ), and extends to lower frequencies. Some decrease in  $\alpha$  should be expected due to data noise (the gray band marks the white noise with amplitude 0.03 nT), especially in the last frequency decade. Notice that sharp peaks at  $f = j \cdot 3.25 \times 10^{-4}$  Hz,  $j = 1, 2, \dots$  are due to instrumental effects. Thus, although the spectral index of magnetic energy is apparently closer to the Iroshnikov–Kraichnan’s power of  $3/2$  (Iroshnikov 1964; Kolmogorov 1965), rather than to the Kolmogorov’s  $5/3$  (Kolmogorov 1941), this issue remains uncertain. We see that anisotropy and compressibility are not negligible at any scale. The spectral magnetic compressibility  $P[|B|]/E_m$  grows with the frequency up to the 0.6 reached at  $10^{-3}$  Hz.

A clear spectral break is present at  $f^* \approx 2 \times 10^{-4}$  Hz ( $\ell^* \approx 10^{-3}$  au), which is comparable with the typical time between intense shears. For  $f > f^*$ , transverse fluctuations have the rms value of  $\approx 8 \times 10^{-3}$  nT. This break separates the high-frequency and intermediate ( $5 \times 10^{-6} \lesssim f \lesssim 10^{-4}$  Hz) ranges, where all components flatten and  $\alpha \lesssim 1$  (the bumps may be due to the data gap artifacts). At lower frequencies  $f \lesssim 10^{-6}$  Hz, a Kolmogorov-like decay is again present, as shown by Burlaga et al. (2018) and Fraternal et al. (2019a). This suggests that the break at  $f^*$  can be attributed to a local energy injection in the kinetic foreshock regions.

#### 4. Summary and Discussion

We demonstrated the presence of intermittency in the anisotropic VLSIM turbulence in the transitional, MHD-to-kinetic frequency range ( $2 \times 10^{-4} \lesssim f \lesssim 10^{-2}$  Hz). The

turbulent cascade exhibits coherent fine-scale structures of mixed transverse/compressible nature, and weak current sheets, possibly originating due to nonlinear wave steepening and breakdown. Enhanced magnetic field fluctuations are detected 44 days after V1 enters the electron foreshock (Gurnett et al. 2015). This suggests the local, shock-mediated nature of this turbulent regime. The observed intermittency is mostly related to transverse fluctuations of amplitude  $\sim 0.1B$  in the presence of small directional discontinuities, compatible with filamentary structures.

It is clear from Figure 1 that the increase in the amplitude of transverse fluctuations at  $c'$  coincides with the recovery in the GCR flux perpendicular to  $B$ , which further results in the flux isotropization (Krimigis et al. 2013; Stone et al. 2013). This is not surprising since the diffusion coefficients strongly correlate with the turbulence level.

It is of interest that the Alfvén velocities in regions I1 and I2 are such that the ratio of the pickup ion (PUI) ring-beam velocity,  $V_r$ , to  $C_A$  is less than 5, which is the condition for efficient electron priming by the lower-hybrid (LHW) wave mechanism (Omelchenko et al. 1989; Cairns & Zank 2002), only if  $V_r$  is derived from the population of neutral H atoms born due to charge exchange in the IHS. Their velocity is about  $100 \text{ km s}^{-1}$ , whereas  $V_r$  is above  $350 \text{ km s}^{-1}$  for the neutral SW. This speaks in favor of the scenario where the LHW generation criterion is always satisfied in the VLISM (see the discussion in Mitchell et al. 2009; Pogorelov et al. 2009). The shocks observed are too weak to substantially affect this criterion. Thus, they are only necessary to generate electron beams in the foreshocks. Remember that those electron beams

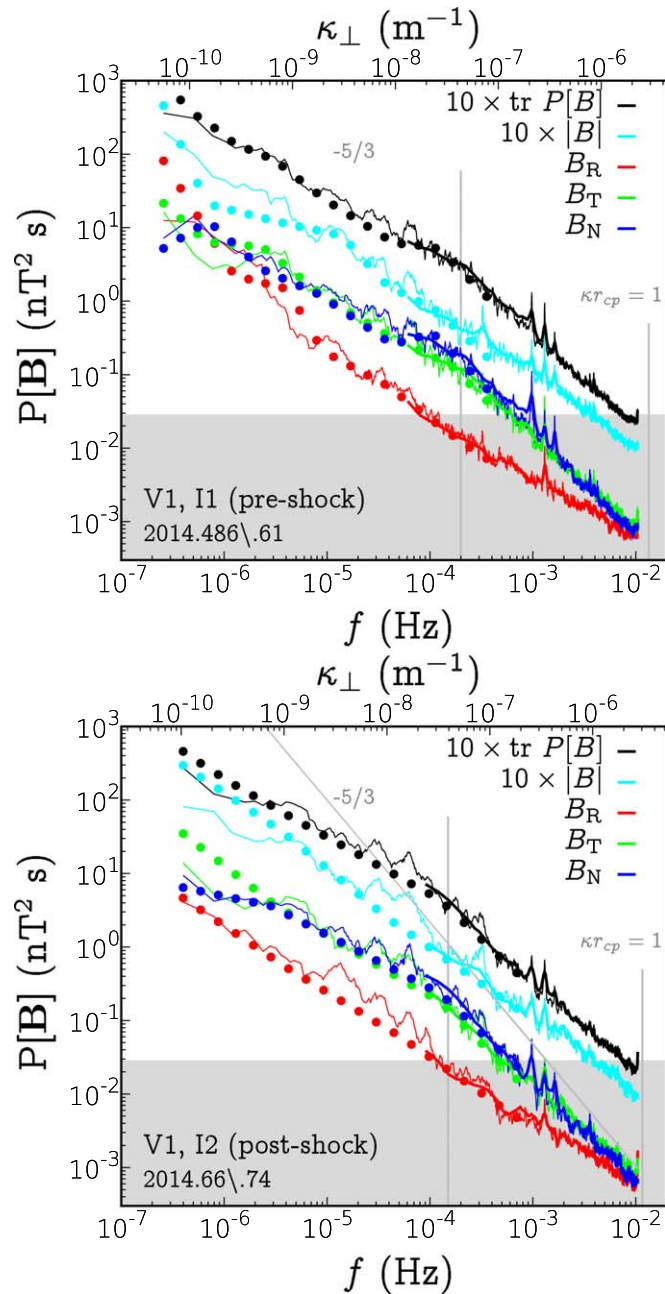


**Figure 5.** Spectra of magnetic field fluctuations in the pre-shock (top panel) and post-shock regions (bottom panel). The results are obtained with three techniques: (i) averaged spectra of gap-free subsets (thick lines); (ii) log-smoothed compressed sensing method (thin lines); and (iii) optimization procedure based on synthetic turbulence sets (bullets).

are required to generate plasma waves and radio emissions observed by V1 in the HBL.

A possibility should be investigated whether kinetic instabilities related to PUIs accelerated in the foreshocks are responsible for the injection of wave power into the broad VLISM spectrum at microscales, resulting in the observed break in the statistics. In the collisionless SW, intense, low-frequency, MHD fluctuations with  $f \sim 0.01\text{--}0.1 f_{cp}$  are known to be generated, e.g., near magnetospheric ion foreshocks (Hoppe et al. 1981; Tsurutani & Stone 1985). Low-intensity shocks with marginally critical Mach numbers can accelerate ions and excite low-frequency waves in a wide foreshock region, even in the quasi-perpendicular configuration (e.g.,

Kajdič et al. 2012). Though infrequently, subcritical shocks with upstream wave precursors (Bavassano-Cattaneo et al. 1986) or reflected ions (Greenstadt & Mellott 1987) have also been found. Magnetic mirroring suggested by Wu (1984) and Jokipii & Kóta (2014) may also serve as a mechanism of the ion foreshock buildup. It is possible that backstreaming ions can propagate along the magnetic field lines from less oblique parts of the shock, which may be as far as 10–20 au from V1. Of importance may be the intermittent character of the observed transition caused by large-scale turbulence and pressure fluctuations, which corrugate the shock surface and affect the shock speed.

We have shown that the VLISM is not featureless on scales below the Coulomb collisional mean free paths  $\lambda^{pp,ee} \sim 0.5$  au for  $T \approx 10,000$  K (Baranov & Ruderman 2013; Mostafavi & Zank 2018) or  $\sim 4$  au for the temperature of 30,000 K and above (Richardson et al. 2019). The VLISM can be considered collisional on scales of  $\sim 100$  au, but kinetic effects are pronounced on the scales considered in this Letter.

This work is supported by NASA grants 80NSSC19K0260, 80NSSC18K1649, and 80NSSC18K1212. L.F.B. was supported by NASA contract 80GSFC19C0012. We acknowledge the NASA Space Physics Data Facility (<https://cohoweb.gsfc.nasa.gov/coho/>).

#### ORCID iDs

Federico Fraternali <https://orcid.org/0000-0002-4700-2762>  
 Nikolai V. Pogorelov <https://orcid.org/0000-0002-6409-2392>  
 Leonard F. Burlaga <https://orcid.org/0000-0002-5569-1553>

#### References

- Baranov, V. B., & Ruderman, M. S. 2013, *MNRAS*, **434**, 3202  
 Bavassano-Cattaneo, M. B., Tsurutani, B. T., Smith, E. J., & Lin, R. P. 1986, *JGR*, **91**, 11929  
 Berdichevsky, D. B. 2009, White Paper, [https://vgrmag.gsfc.nasa.gov/20151017BzPLeEstimates\\_wMAGCAL.pdf](https://vgrmag.gsfc.nasa.gov/20151017BzPLeEstimates_wMAGCAL.pdf)  
 Bruno, R., & Carbone, V. 2013, *LRSP*, **10**, 2  
 Burlaga, L., Florinski, V., & Ness, N. 2015, *ApJL*, **804**, L31  
 Burlaga, L., & Ness, N. 2011, *JGRA*, **116**, A05102  
 Burlaga, L., & Ness, N. 2016, *ApJ*, **829**, 134  
 Burlaga, L., Ness, N. F., Berdichevsky, D., et al. 2019a, *NatAs*, **3**, 1007  
 Burlaga, L. F. 1969, *SoPh*, **7**, 54  
 Burlaga, L. F. 1995, *Interplanetary Magnetohydrodynamics* (Oxford: Oxford Univ. Press)  
 Burlaga, L. F., Florinski, V., & Ness, N. F. 2018, *ApJ*, **854**, 20  
 Burlaga, L. F., Lemaire, J. F., & Turner, J. M. 1977, *JGR*, **82**, 3191  
 Burlaga, L. F., Ness, N. F., Berdichevsky, D. B., et al. 2019b, *ApJ*, **877**, 31  
 Burlaga, L. F., Ness, N. F., & Stone, E. C. 2013, *Sci*, **341**, 147  
 Cairns, I. H., & Zank, G. P. 2002, *GeoRL*, **29**, 1143  
 Fraternali, F., Pogorelov, N. V., Richardson, J. D., & Tordella, D. 2019a, *ApJ*, **872**, 40  
 Fraternali, F., Pogorelov, N. V., Richardson, J. D., & Tordella, D. 2019b, *JPhCS*, **1225**, 012006  
 Gallana, L., Fraternali, F., Iovieno, M., et al. 2016, *JGRA*, **121**, 3905  
 Greco, A., Chuychai, P., Matthaeus, W. H., Servidio, S., & Dmitruk, P. 2008, *GeoRL*, **35**, L19111  
 Greenstadt, E. W., & Mellott, M. M. 1987, *JGRA*, **92**, 4730  
 Gurnett, D. A., Kurth, W. S., Burlaga, L. F., & Ness, N. F. 2013, *Sci*, **341**, 1489  
 Gurnett, D. A., Kurth, W. S., Stone, E. C., et al. 2015, *ApJ*, **809**, 121  
 Hoppe, M. M., Russell, C. T., Frank, L. A., et al. 1981, *JGRA*, **86**, 4471  
 Iroshnikov, P. S. 1964, *SvA*, **7**, 566  
 Jokipii, J. R., & Kóta, J. 2014, *ApJL*, **794**, L4  
 Kajdič, P., Blanco-Cano, X., Aguilar-Rodríguez, E., et al. 2012, *JGRA*, **117**, A06103

- Kim, T. K., Pogorelov, N. V., & Burlaga, L. F. 2017, [ApJL](#), **843**, L32
- Kolmogorov, A. N. 1941, *DoSSR*, **30**, 301
- Kolmogorov, A. N. 1965, [PhFl](#), **8**, 1385
- Krimigis, S. M., Decker, R. M., Roelof, E. C., et al. 2013, [Sci](#), **341**, 144
- Matsukiyo, S., Noumi, T., Zank, G. P., et al. 2019, [ApJ](#), **888**, 1
- Matthaeus, W. H., Wan, M., Servidio, S., et al. 2015, [RSPTA](#), **373**, 20140154
- Mitchell, J. J., Cairns, I. H., & Heerikhuisen, J. 2009, [GeoRL](#), **36**, L12109
- Mostafavi, P., & Zank, G. 2018, [ApJL](#), **854**, L15
- Omelchenko, Y. A., Sagdeev, R. A., Shapiro, V. D., & Shevchenko, V. I. 1989, *Sov. J. Plasma Phys.*, **15**, 427
- Pogorelov, N. V., Borovikov, S. N., Heerikhuisen, J., & Zhang, M. 2015, [ApJL](#), **812**, L6
- Pogorelov, N. V., Fichtner, H., Czechowski, A., et al. 2017a, [SSRv](#), **212**, 193
- Pogorelov, N. V., Heerikhuisen, J., Mitchell, J. J., Cairns, I. H., & Zank, G. P. 2009, [ApJL](#), **695**, L31
- Pogorelov, N. V., Heerikhuisen, J., Roytershteyn, V., et al. 2017b, [ApJ](#), **845**, 9
- Richardson, J. D. 2016, in *AIP Conf. Proc.* 1720, Solar Wind 14, ed. L. Wang et al. (Melville, NY: AIP), 080001
- Richardson, J. D., Belcher, J. W., Garcia-Galindo, P., & Burlaga, L. F. 2019, [NatAs](#), **3**, 1019
- Stone, E. C., Cummings, A. C., McDonald, F. B., et al. 2013, [Sci](#), **341**, 150
- Taylor, G. I. 1938, [RSPSA](#), **164**, 476
- Tsallis, C. 1988, [JSP](#), **52**, 479
- Tsurutani, B. T., & Stone, R. G. 1985, *Collisionless Shocks in the Heliosphere: Reviews of Current Research* (Washington, DC: AGU)
- Wu, C. S. 1984, [JGR](#), **89**, 8857
- Zank, G. 2015, [ARA&A](#), **53**, 449
- Zank, G. P., Du, S., & Hunana, P. 2017, [ApJ](#), **842**, 114
- Zank, G. P., Nakanotani, M., & Webb, G. M. 2019, [ApJ](#), **887**, 116